

Distinct impact of PI(4)P flux in regulating PI(4,5)P₂ steady states and oscillations

X. J. Xu^a, C. S. Tong^b, and M. Wu^b

This manuscript was compiled on July 8, 2025

Plasma membrane (PM) phosphatidylinositol 4,5-bisphosphate [PI(4,5)P₂] regulates indispensable processes such as exocytosis, endocytosis and actin cytoskeleton remodeling in eukaryotic cells. Since phosphatidylinositol 4-phosphate [PI(4)P] has been long regarded as the primary precursor of PI(4,5)P₂, perturbing PM PI(4)P is expected to impact the dynamics of PM PI(4,5)P₂. Yet, recent evidence suggests that PM PI(4)P has a limited role in the synthesis and function of PI(4,5)P₂. In this paper, we address this puzzling discrepancy by studying the collective dynamics of PM PI(4)P and PI(4,5)₂ through a dynamical systems conceptual framework. Leveraging live-cell imaging, we observed periodic traveling waves of PI(4)P on the PM of mast cells, challenging the notion that this precursor lipid only exist at steady state levels. We then found that a reduction in PM PI(4)P synthesis rate attenuated PI(4,5)P₂ oscillation amplitude while conserving space-average PM steady state level. We assessed the functional consequence PI(4,5)P₂ oscillation amplitude by examining its interplay with Rho GTPase Cdc42, which cooperatively regulates the actin cytoskeleton with PI(4,5)P₂. We showed that both PM PI(4)P and PI(4,5)P₂ oscillations are coupled to oscillations of membrane-bound active Cdc42. Finally, we demonstrated that lowering PM PI(4)P synthesis rate alone was sufficient to reversibly eliminate oscillations of active Cdc42. Beyond the steady state depiction, cortical oscillations require a critical PI(4)P synthesis rate.

phosphoinositides | oscillations | Rho GTPase

Phosphoinositides orchestrate a myriad of physiological functions by defining the identity of subcellular membrane compartments in eukaryotic cells (1, 2). Among the phosphoinositides, phosphatidylinositol 4,5-bisphosphate [PI(4,5)P₂] is a critical regulator of signal transduction, intracellular transport, and cytoskeletal organization at the plasma membrane (PM). The proteins associated with these functions are recruited from the cytosol to the PM via interactions with specific phosphorylated inositol headgroup protruding from the cytosolic leaflet (3, 4). The *myo*-inositol ring permits phosphorylation on the 3', 4' and 5' positions, yielding seven unique phosphoinositides with different binding specificities and affinities to proteins (2, 5, 6). The spatial control of the generation and metabolism of each phosphoinositide are regulated by specific lipid kinases and phosphatases (7). For instance, PI(4,5)P₂ is synthesized through two enzymatic reactions in which phosphatidylinositol (PI) is first phosphorylated by a PI 4-kinase to produce phosphatidylinositol 4-phosphate [PI(4)P], which is then converted to PI(4,5)P₂ by a 5-kinase (8).

Despite being the primary substrate for PI(4,5)P₂ synthesis, PI(4)P can be depleted dramatically at the plasma membrane with little to no impact on PI(4,5)P₂ levels and function (9–12). This counterintuitive result has sparked a variety of proposed explanations for the homeostasis of steady state PM PI(4,5)₂ levels, including contributions from the Golgi pool of PI(4)P (13, 14), PI(4)P exchange at membrane contact sites mediated by ORP proteins (15, 16) and regulation via a minor reaction pathway through type II PIP kinases (PI5P 4-kinases) (17). On the other hand, PI(4)P synthesis by PI 4-kinases has also been suggested to be important for the replenishment and localization of PI(4,5)P₂ (18, 19) as well as a multitude of cellular signaling processes (20). For instance, the catalytic activity of PI4KIII α (PI4KA), the major PI 4-kinase responsible producing PM PI(4)P, is required for physiological functions such as IgE receptor signaling (21), wing development in *Drosophila melanogaster* (22) and pituitary hormone secretion in *Rattus norvegicus* (23). Taken together, we reasoned that these seemingly conflicting observations reflect the possibility that PM PI(4)P flux has distinct roles in regulating PI(4,5)P₂ steady states versus oscillations.

Beyond the steady state regime, the available pool of PI(4,5)P₂ can undergo oscillations alongside calcium and actin oscillations during antigen stimulated exo-

Significance Statement

Membrane identity in eukaryotic cells is defined by the phosphoinositide family of phospholipids, with phosphatidylinositol 4,5-bisphosphate [PI(4,5)P₂] serving as the key signaling lipid that resides on and defines the inner leaflet of the plasma membrane (PM). There, PI(4,5)P₂ plays indispensable roles such as intracellular transport and morphogenesis. Despite PI(4,5)P₂'s central role, how its precursor PI(4)P drives its dynamics remains unclear. In this paper, we found that PM PI(4)P, previously regarded as a static pool, can also exist as periodic oscillations. We then showed that the rate of PM PI(4)P synthesis is critical for maintaining PM PI(4,5)P₂ oscillations. The wave nature of phosphoinositides highlight the need to understand cellular membranes in a broader dynamical regime.

Author affiliations: ^aDepartment of Physics, Yale University, New Haven, Connecticut 06511; ^bDepartment of Cell Biology, Yale University, New Haven, Connecticut 06510

cytosis in mast cells (24–26). Yet, there is no account for the impact of PM PI(4)P depletion on PM PI(4,5)₂ oscillations. Thus, in this study, we focus on elucidating an account of how PI(4)P influx impacts PI(4,5)₂ oscillations, where progress is hindered by at least two key challenges. First, selective yet minimally perturbative detection of phosphoinositides in living cells remains technically challenging, owing to their low abundance in membranes and high rate of metabolic turnover. Second, past studies often relied on endpoint or low temporal resolution measurements, which obscure the fast biochemical reactions that drive phosphoinositide metabolism. Recent developments of fluorescent biosensors made it possible to overcome the first challenge (12, 27). Thus it is necessary to resolve the second challenge in order to probe the rapid turnover of PI(4)P.

We hypothesized that the robust PI(4,5)P₂ behavior under PI(4)P depletion arises from a mismatch between the timescale of lipid perturbation measurements and the rapid dynamics of the underlying enzymatic reactions. For instance, biological enzymes can exhibit catalytic rates on the timescale of milliseconds (10^{-1} to 10^{-3} seconds) (28, 29). In contrast, most experimental designs involve lipid quantification minutes (10^2 to 10^3 seconds) after perturbation and rely on single micrographs that integrate over long timescales (9–11). In addition, these experimental designs are based on fibroblasts or epithelial cells (10, 11, 13, 30, 31). Yet, as early as the 1950s, discoveries in phosphoinositide metabolism were first made in pancreatic tissue slices, which are specialized for enzyme secretion and exhibited dramatic phosphoinositide turnover upon acute stimulation (32, 33). To bridge the gap, we utilized a classic granule-secreting mast cell as a model system in combination with modern fluorescent lipid and GTPase sensors. Using total internal reflection fluorescence (TIRF) microscopy, we imaged PI(4)P lipid sensors at the PM of mast cells with sub-second acquisition rates, more closely matching the timescale of lipid enzymatic reactions. This approach enabled us to observe a previously inaccessible dynamical phenomenon of traveling waves of PM PI(4)P sensor intensity. We then demonstrated that there is a critical rate of PM PI(4)P synthesis that tunes PI(4,5)P₂ oscillation amplitude without affecting PI(4,5)P₂ space-average PM intensity. We wondered what is the cellular consequence of PI(4,5)P₂ oscillation amplitude attenuation on downstream effector proteins. Thus we considered the small Rho GTPase Cdc42 that has a well-known association with PI(4,5)P₂ and a key role in regulating the actin cytoskeleton (34, 35). We found that a reduction of PI(4,5)P₂ oscillation amplitude leads to dampening of membrane-bound active Cdc42 oscillations. In this paper, we demonstrated how we can gain insights by considering a broader dynamical regime, from steady states to oscillations.

Results

Plasma membrane PI(4)P exists in traveling waves. To investigate the role of PM PI(4)P in regulating PM PI(4,5)P₂ levels, we used time-lapse total internal reflection fluorescence (TIRF) microscopy to visualize the dynamics of PM PI(4)P with sub-second temporal resolution (Fig. 1A). We chose the rat basophilic leukemia (RBL) cells as a mast cell model system due to their specialized antigen-stimulated secretory response and dynamic membrane trafficking processes, such

as antigen-stimulated oscillations of PM PI(4,5)P₂ and coordinated endocytosis (24, 36). We stimulated RBL cells with an antigen dinitrophenyl (DNP-BSA) to elicit a consistent physiological condition for imaging PM PI(4)P (see details in Methods section). To detect PM PI(4)P with high specificity, we over-expressed in RBL cells the PI(4)P binding domain of SidM (P4M) fused to a near-infrared fluorescent protein (iRFP) at the N-terminus (12, 37). Compared to other PI(4)P sensors constructed from OSBP, FAPP and OSH2, P4M is unique in that PI(4)P is necessary and sufficient for specific binding to membrane as indicated by the specific localization of this probe to the PM (38–40).

For the best signal-to-noise ratio, we optimized the imaging of the iRFP-P4M sensor in RBL cells by adjusting the evanescent field to have a penetration depth of 100–120 nm with a laser exposure duration of 50–150 ms (Fig. 1A). Upon antigen stimulation, time-lapse TIRF movies of RBL cells expressing exogenous iRFP-P4M revealed coherent traveling wavefronts of iRFP-P4M fluorescence (Fig. 1B). The sensor fluorescence intensity is interpreted to reflect the available pool of unbound PM PI(4)P, rather than the sequestered pool or the total pool of lipids. By taking a 1-dimensional slice of the image stack across the center of the cell, kymographs and stacked line plots were generated to visualize the oscillatory nature of the iRFP-P4M fluorescence as a readout of traveling fluorescence wavefronts (Fig. 1B–C). By performing a discrete fast Fourier transform on the fluorescence time series, we quantified the periodicity of the iRFP-P4M oscillation to be 27.4 ± 0.5 seconds (Fig. 1D). We also checked that choosing different regions of interest (ROI) on the same cell would only change the oscillatory phase but not the periodicity (Fig. S1). For clarification, oscillation refers to the time series oscillations, without the spatial dimensions, whereas traveling waves refers to the propagating wavefront of iRFP-P4M fluorescence in time as well as in two spatial dimensions. After determining the oscillation period of iRFP-P4M to be on the order of 10^1 seconds, we found that an image acquisition rate between 0.5 and 4 seconds is sufficient to capture the PI(4)P dynamics.

To ensure that the observed traveling waves of iRFP-P4M were not due to an artifact caused by a loss of TIRF signal, we imaged antigen-stimulated RBL cells expressing iRFP-P4M alongside a cytosolic enhanced green fluorescent protein (EGFP) (Fig. S2A). The oscillations were observed only in the fluorescence signal of the iRFP-P4M sensor, but not in the fluorescence of cytosolic EGFP. This finding suggests that PM PI(4)P can not only exist at steady state, but also as oscillations. This prompted us to reevaluate how the precursor PI(4)P can regulate PI(4,5)P₂ oscillations.

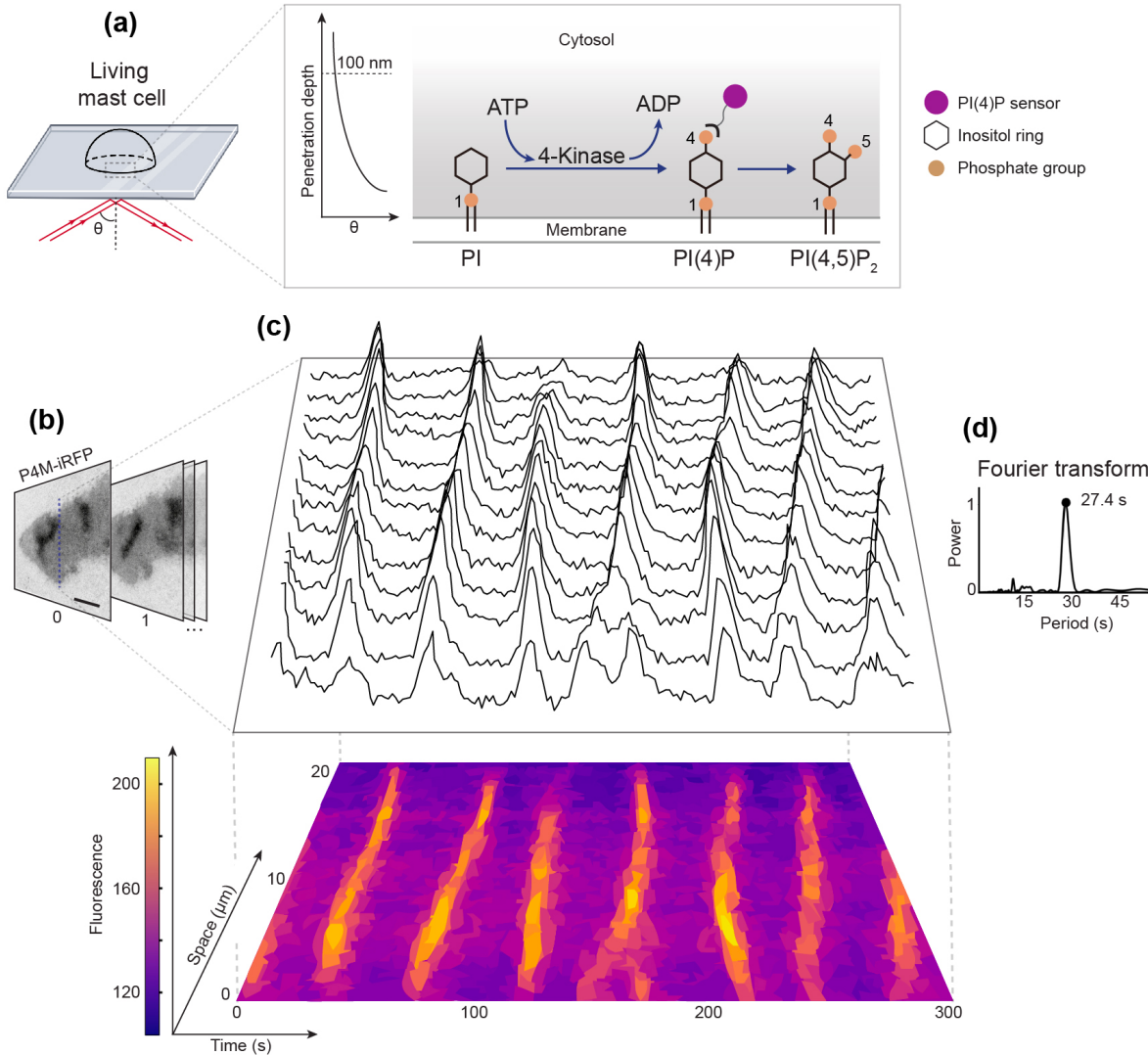
Inhibition of PI4KIII α impacts PI(4,5)P₂ oscillations but not steady state level. To evaluate the role of PI(4)P has on PI(4,5)P₂ oscillations at the PM, we imaged PI(4,5)P₂ oscillations with a method in line with our past work (24, 26). We utilized the PH domain of PLC δ fused to an iRFP at the N-terminus (iRFP-PH_{PLC δ}) to detect PM PI(4,5)P₂ traveling waves after antigen stimulation in RBL cells, with cytosolic EGFP control (Fig. S2B). We utilized the same iRFP-P4M sensor imaging protocol as the previous section and perturbed the rate of PI(4)P synthesis. To achieve this effect, we used the potent chemical inhibitor GSK-A1 (11) to acutely inhibit the catalytic activity of the PI 4-kinase PI4KIII α , the highly

249
250
251
252
253
254
255
256

311
312
313
314
315
316
317
318

257
258
259
260
261
262
263
264
265
266
267

319
320
321
322
323
324
325
326
327
328
329



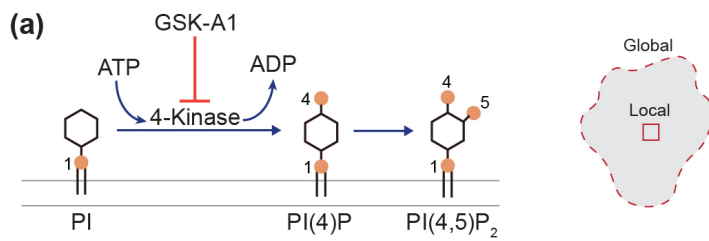
295 **Fig. 1. Time-lapse fluorescence imaging reveals PI(4)P traveling waves in living mast cells.** (a) Experimental schematic of TIRF imaging of living mast cells. A laser angle
296 θ-dependent evanescent field (~100 nm penetration depth) selectively excites PI(4)P sensor fluorophores above the plasma membrane (PM) of an adherent RBL mast cell.
297 Molecular diagram of the enzymatic reactions shows the canonical synthetic pathway of the PI → PI(4)P → PI(4,5)P₂. The catalytic domain of 4-kinase PI4KIIIα transfers a
298 phosphate group from ATP to PI, generating PI(4)P. The genetically encoded PI(4)P sensor iRFP-P4M (purple) selectively binds to PM PI(4)P (orange, phosphate groups; gray,
299 inositol). (b) Representative TIRF micrographs (300 by 300 pixels) of iRFP-P4M fluorescence in a single cell at two consecutive time points in a image stack. The dashed blue
300 line marks the axis used to construct the stacked line plot and kymograph. Scale bar: 10 μm. (c) Fluorescence intensity stacked lined plots and space-time kymographs display
301 the coherent traveling wave fronts. Top: stacked line plots of one-dimensional fluorescence intensity time series extracted from discretized binning of the image stack.
302 Bottom: space-time (x-t) kymograph generated from the dashed line in (b) reveals diagonally propagating bands of high fluorescence (warm colors), interpreted as PI(4)P traveling
303 waves on the PM. (d) Discrete fast Fourier transform (FFT) of the fluorescence intensity time series in (c) shows a single dominant spectral peak defining the oscillation period
304 to be 27.4 s.

305
306
307
308
309
310

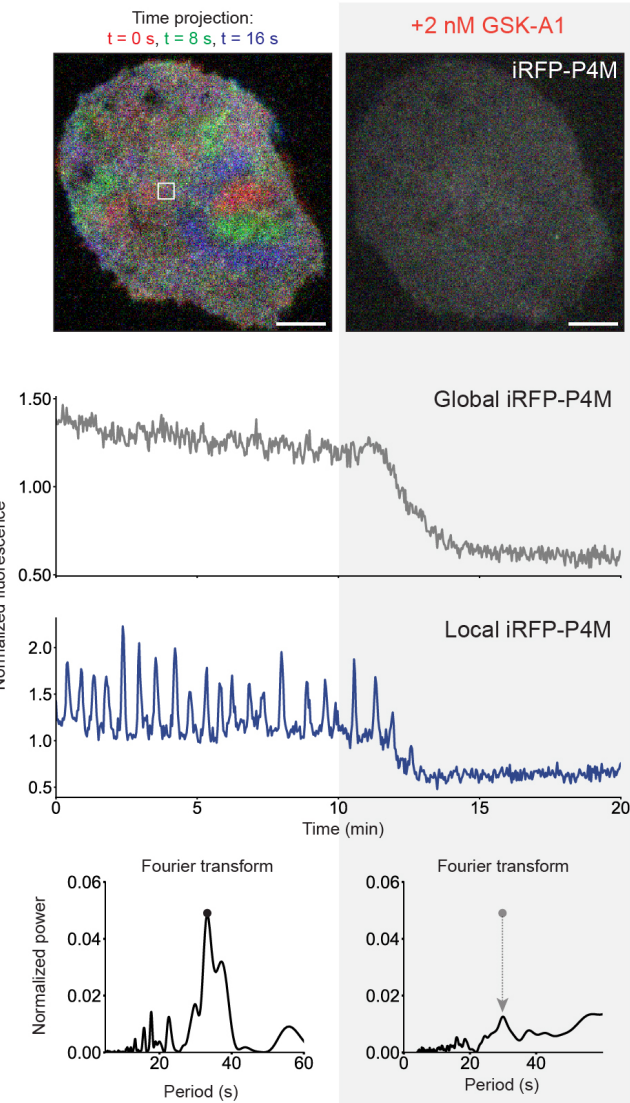
357
358
359
360
361
362
363
364
365
366
367
368
369
370
371
372

373
374
375
376
377
378
379
380
381
382
383
384

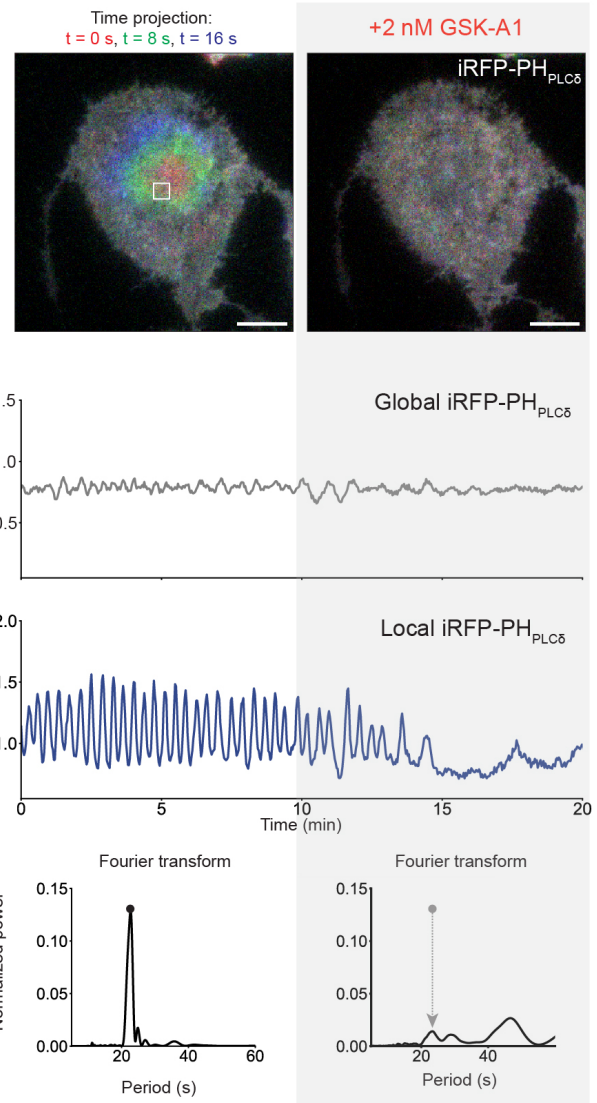
435
436
437
438
439
440
441
442
443
444
445
446



(b) PI(4)P



(c) PI(4,5)P₂



426 **Fig. 2. PIP 4-Kinase perturbation lowers the global baseline intensity of PI(4)P but not that of PI(4,5)P₂.** (a) Schematic of lipid metabolism and chemical perturbation.
427 Schematic showing local (20 by 20 pixel) versus global (whole cell) region of interest for plotting fluorescence intensities of a cell. (b) Annihilation of iRFP-P4M oscillations and
428 reduction of baseline intensity induced by 2 nM of GSK-A1 inhibitor added at the 10th minute of the time series. Top, time projection images of iRFP-P4M before and after
429 GSK-A1 addition. Middle, time series plots of whole-cell-averaged global versus local iRFP-P4M fluorescence. Bottom, discrete FFTs of the local time series before (left) and
430 after (right) 2 nM of GSK-A1 treatment show that the dominant spectral peak is abolished. (c) Annihilation of iRFP-PH_{PLCδ} oscillations without a reduction of baseline global
431 intensity induced by 2 nM of GSK-A1 inhibitor. Top, time projection images of iRFP-PH_{PLCδ} before and after GSK-A1 addition. Middle, time series plots of whole-cell-averaged
432 global versus local iRFP-PH_{PLCδ} fluorescence. Bottom, same as (b). Scale bars: 10 μ m.

488
489
490
491
492
493
494
495
496

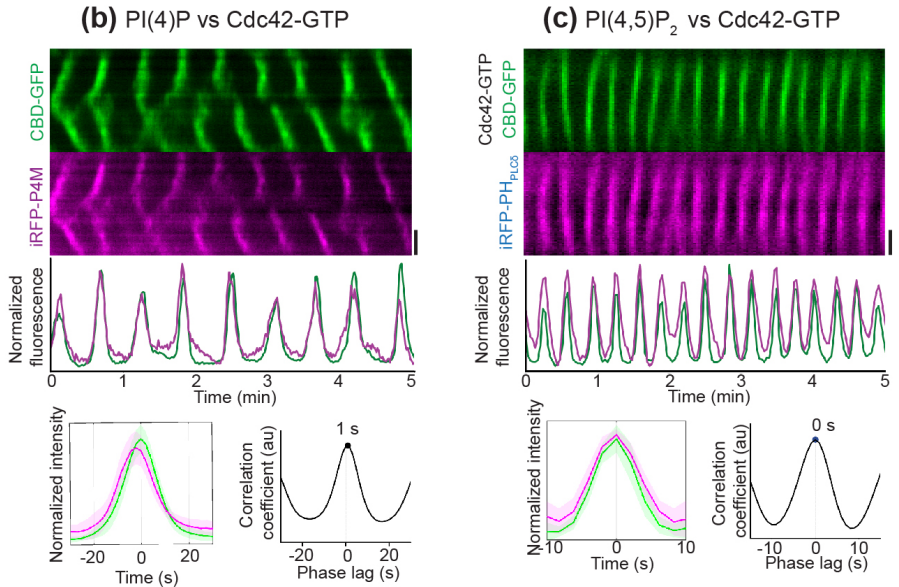
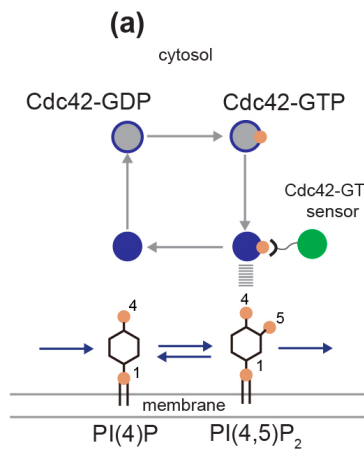
497
498
499
500
501
502
503
504
505
506
507
508
509
510
511
512
513
514
515
516
517

Fig. 3. Active Cdc42 traveling waves are coupled to PI(4)P and PI(4,5)P₂ waves. (a) Schematic is drawn to show the presence of the two coupled Cdc42 and phosphoinositide molecular networks, rather than to show exact GTPase recruitment and activation mechanism. The active Cdc42 sensor CBD-GFP detects membrane-bound Cdc42-GTP. (b) Dual-color TIRF imaging of Cdc42-GTP (CBD-GFP, green) and PI(4)P (iRFP-P4M, magenta). Kymograph from a 5 minute movie shows co-localized traveling wavefronts of the CBD-GFP and iRFP-P4M sensors. Time series of normalized fluorescence illustrate the coinciding oscillations. Bottom left: cross-correlation of the two time series. Bottom right: average aligned peak intensity (line) from all oscillation peaks (shaded) show a minor offset of peaks. (c) Same analysis as (b) for dual-color TIRF imaging of Cdc42-GTP (CBD-GFP, green) and PI(4,5)P₂ (iRFP-PH_{PLCδ}, magenta). Kymograph vertical spatial scale bar: 10 μm for (b) and (c).

524 conserved enzyme thought to be responsible for the majority
525 of PI(4)P synthesis on the PM (9, 41–44). GSK-A1 blocks
526 the ATP-binding site of the PI4KIIIα catalytic domain (45)
527 and induces allosteric conformational changes throughout
528 the kinase domain (46), therefore inhibiting PI4KIIIα on
529 the seconds timescale. We conducted an acute perturbation
530 experiment by acutely inhibiting the 4-kinase PI4KIIIα with
531 GSK-A1 and observing the corresponding effect on PI(4)P
532 and PI(4,5)P₂ oscillations respectively (Fig. 2A left).

533 Upon acute inhibition of PI4KIIIα activity with 2 nM
534 GSK-A1 after 10 minutes of observing traveling waves, we
535 observed a rapid and dramatic attenuation of iRFP-P4M
536 oscillations at the PM (Fig. 2B). This was accompanied by
537 a substantial decrease in global space-average iRFP-P4M
538 fluorescence intensity on the PM, indicating depletion of the
539 steady-state availability of PI(4)P. Discrete fast Fourier trans-
540 form analysis confirmed the loss of a dominant periodicity
541 peak (Fig 2B bottom), and kymographs showed cessation
542 of traveling iRFP-P4M waves (Fig. S3). Importantly, we
543 make a key distinction between global versus local lipid
544 level inferred from sensor fluorescence intensity (Fig. 2A
545 right). A similar loss of oscillatory behavior was observed
546 for PI(4,5)P₂, as measured by the iRFP-PH_{PLCδ} sensor.
547 Notably, however, the global space-average PM intensity
548 of PI(4,5)P₂ sensors remained largely unchanged following
549 PI4KIIIα inhibition (Fig. 2C). Our results here indicate that
550 while steady-state PI(4,5)P₂ levels are preserved, PI(4,5)P₂
551 oscillations amplitude is highly sensitive to the rate of PM
552 PI(4)P synthesis.

553 **Phosphoinositide and Rho GTPase Cdc42 traveling waves**
554 **are spatiotemporally coupled.** We further hypothesized that
555 oscillations of PI(4)P and PI(4,5)P₂ on the PM may have
556 some functional consequence independently of the global
557

558 availability of PI(4,5)P₂. A well-characterized PI(4,5)P₂
559 effector on the PM is the small Rho GTPase Cdc42, which
560 plays a role on cytoskeletal actin polymerization through
561 interactions with formins and Arp2/3 (47, 48). The activity
562 of Cdc42 and its membrane-bound GEFs are known to have
563 dependence on PI(4,5)P₂ containing membranes *in vitro* (49–
564 51) (Fig. 3A). Therefore we examined in living RBL cells
565 the dynamics of Cdc42 alongside PI(4)P or PI(4,5)P₂ with
566 dual-color TIRF imaging.

567 We visualized active GTP-bound Cdc42 using the Cdc42
568 binding domain (CBD) of Wiskott–Aldrich syndrome protein
569 (WASP) fused with a GFP at the C-terminus (CBD-GFP)
570 (52). Live-cell imaging revealed robust oscillations of CBD-
571 GFP on the PM, closely synchronized with iRFP-P4M
572 oscillations (Fig. 3B). Both iRFP-P4M and CBD-GFP oscil-
573 lations displayed a consistent periodicity, as demonstrated by
574 kymographs and fluorescence intensity time-series analysis
575 (Fig. 3B, upper panels). Cross-correlation analysis indicated
576 that the iRFP-P4M and CBD-GFP oscillations occurred
577 within an acquisition frame (~1s) (Fig. 3B). Similarly, we
578 performed the same analysis for iRFP-PH_{PLCδ} and CBD-
579 GFP (Fig. 3C). We have demonstrated that PI(4)P and
580 PI(4,5)P₂ oscillations are spatiotemporally aligned with cycles
581 of membrane-bound active Cdc42, providing a promising
582 link between dynamic phosphoinositide patterning and Rho
583 GTPase-mediated effector function.

584 **Perturbation to rate of PI(4)P synthesis reversibly attenuates**
585 **Cdc42 oscillations.** To test whether PIP 4-kinase activity
586 modulates the amplitude of Cdc42 oscillations, we inferred
587 Cdc42-GTP levels in single cells before and after acute addi-
588 tion of 2 nM GSK-A1. In the absence of the inhibitor, robust
589 CBD-GFP and iRFP-PH_{PLCδ} oscillations were observed,
590 characterized by a consistent peak amplitude and regular
591

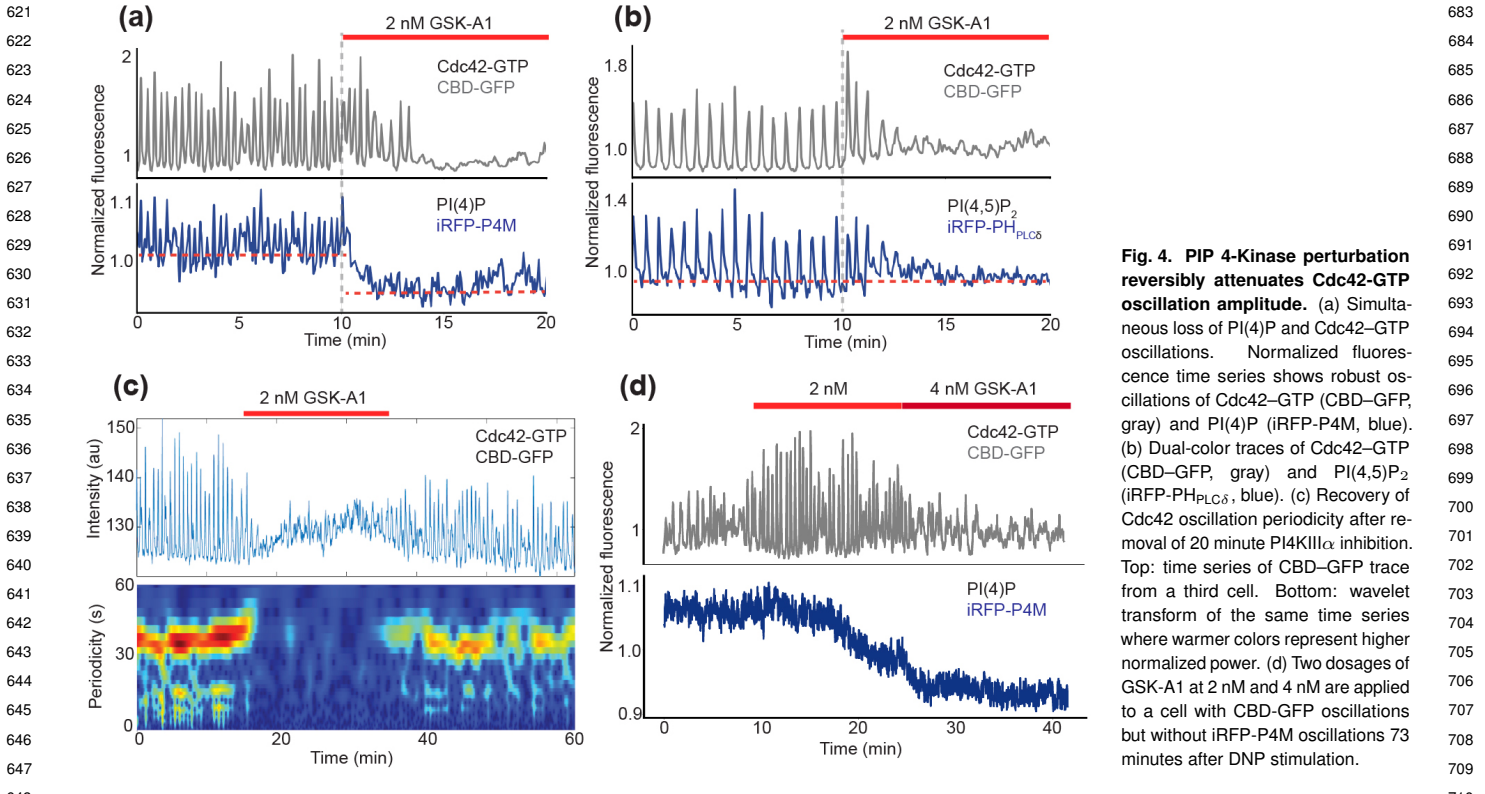


Fig. 4. PIP 4-Kinase perturbation reversibly attenuates Cdc42-GTP oscillation amplitude. (a) Simultaneous loss of PI(4)P and Cdc42–GTP oscillations. Normalized fluorescence time series shows robust oscillations of Cdc42–GTP (CBD–GFP, gray) and PI(4)P (iRFP–P4M, blue). (b) Dual-color traces of Cdc42–GTP (CBD–GFP, gray) and PI(4,5)P₂ (iRFP–PH_{PLCδ}, blue). (c) Recovery of Cdc42 oscillation periodicity after removal of 20 minute PI4KIIIα inhibition. Top: time series of CBD–GFP trace from a third cell. Bottom: wavelet transform of the same time series where warmer colors represent higher normalized power. (d) Two dosages of GSK-A1 at 2 nM and 4 nM are applied to a cell with CBD–GFP oscillations but without iRFP–P4M oscillations 73 minutes after DNP stimulation.

periodicity (Fig. 4A). Addition of 2 nM GSK-A1 (blue bar; start indicated by gray dashed line) drives a rapid, global drop in PI(4)P (red dashed line) and abolishes local PI(4)P oscillations within 90 s. Cdc42–GTP oscillations decay with slightly more delay. On the other hand, 2 nM GSK-A1 eliminates both iRFP–PH_{PLCδ} and CBD–GFP oscillations with a 2 minute delay. Meanwhile, the baseline PI(4,5)P₂ level (red dashed line) stays flat. As shown in Fig. 4A–B, in cells co-expressing Cdc42 and lipid sensors, PI4KIIIα inhibition terminated iRFP–P4M, iRFP–PH_{PLCδ}, as well as CBD–GFP oscillations. Therefore, a critical rate of PM PI(4)P synthesis is required to maintain oscillations of Cdc42 recruitment, activation and retention on the PM.

Notably, this effect was reversible. We performed the same experiment except after CBD–GFP oscillations are damped, we washed out the 2 nM GSK-A1. CBD–GFP oscillations are restored in 2 minutes with comparable amplitude and frequency (Fig. 4C). Wavelet analysis further corroborated these findings by illustrating a pronounced decrease in oscillation power about 1 minute after GSK-A1 addition, while the dominant frequency band persisted after GSK-A1 washout. Reversibility reinforces that the amplitude attenuation was specifically linked to PI4KIIIα inhibition rather than other indirect perturbative effects. In a special case where a cell does not exhibit CBD–GFP nor iRFP–P4M oscillations, the application of 2 nM in fact induced the onset of CBD–GFP oscillations while simultaneously depleting iRFP–P4M intensity (Fig. 4D). By adding a second dosage of GSK-A1 to increase the concentration to 4 nM, the CBD–GFP oscillations terminated again as we would expect in comparison to Fig. 4A. These results demonstrate that PIP 4-kinase activity is essential for maintaining the full amplitude of Cdc42–GTP oscillations.

Discussion

Collectively, these results suggest that there is a critical rate of PI(4)P synthesis from PI4KIIIα required to sustain PI(4,5)P₂ and Cdc42 oscillations—highlighting a previously underappreciated distinction between the regulation of steady state lipid densities and lipid oscillations at the PM. We elucidated that PI(4)P synthesis rate determines PI(4,5)P₂ oscillation amplitude in the secretion specialist mast cell. In addition, our observation of unchanging global space-average PM PI(4,5)P₂ under PI4KIIIα inhibition is in agreement with previous findings by Hammond et al., who reported that PI(4)P depletion via PJ-Sac recruitment does not significantly alter total PM PI(4,5)P₂ levels (10).

This work relied on the approach of framing membrane trafficking problems as a system of enzymatic reactions with nonlinear feedback loops which captures a wider range of dynamics in phosphoinositide metabolism, such as biochemical oscillations (53) and bistability (54). Such an approach benefits from the synergy between modern advances in both mathematical frameworks (55–57) and live cell biosensor measurements (40). For instance, recently developed ORP9-based PI(4)P sensors (58) provide improved detection of PM PI(4)P and suitability for investigating PI(4)P dynamics in conjunction with endoplasmic reticulum–plasma membrane contact sites, where many phosphoinositide metabolic processes take place (59–63).

In this paper, we found that not only are membrane-bound oscillations of active Rho GTPase Cdc42 synchronized with both PI(4)P and PI(4,5)P₂ waves, they are also highly sensitive to a reduction of PM PI(4)P synthesis rate. The patterning of Rho GTPases is usually thought to be driven by the canonical regulators: guanine nucleotide exchange

745 factors (GEFs), GTPase-activating proteins (GAPs), and
746 guanine nucleotide dissociation inhibitors (GDIs) (64). Here
747 we demonstrated the acute impact of PI4KIII α inhibition
748 on Cdc42 traveling waves, suggesting the need to include
749 phosphoinositides in the descriptions of Rho GTPase pattern
750 formation. In fact, the minimal reconstitution of Cdc42
751 traveling waves *in vitro* remains an open problem, and
752 a potential solution may reside in understanding the key
753 interactions and feedbacks between phosphoinositides, PIP
754 enzymes and Cdc42 along with its regulators.

755 In conclusion, our investigation illustrates the key insights
756 to be gained from membrane trafficking questions in terms of
757 dynamic reaction rates, rather than as steady state levels and
758 linear synthesis pathways. Accordingly, experimental mea-
759 surements must capture these processes on relevant timescales
760 to retain critical dynamical information. Furthermore, we
761 demonstrated that a phosphoinositide enzyme impacts the
762 spatiotemporal patterning of Rho GTPase Cdc42, in addition
763 to the canonical GTPase regulators. More broadly, our
764 results point towards a dynamical systems approach for
765 understanding lipid metabolism and lipid-protein interactions
766 underlying fundamental cellular processes.

767 Materials and Methods

768 **Materials.** The rat basophilic leukemia (RBL-2H3) mast cell
769 line was a kind gift from Barbara Baird and David Holowka
770 (Cornell University, Ithaca, NY). The following reagents were
771 purchased from commercial sources: mouse monoclonal anti-
772 dinitrophenol (DNP) IgE antibody and GSK-A1 from Sigma-
773 Aldrich; albumin from bovine serum albumin covalently
774 attached to dinitrophenyl (DNP-BSA, Catalog #A23018)
775 and Geneticin Selective Antibiotic G418 Sulfate from Thermo
776 Fisher Scientific. The following protein constructs iRFP-P4M
777 (12) (Addgene #51470) and iRFP-PH_{PLC δ} (65) (Addgene
778 #66841) were kind gifts from Tamas Balla and Pietro de
779 Camilli (Yale University, New Haven, CT) respectively. CBD-
780 GFP was previously generated (24) by cloning pET23-CBD-
781 (-PP)-EGFP (Addgene #12597) into pEGFP-N1 vector with
782 restriction sites XhoI and BamH1. For experiments utilizing
783 the CBD-GFP sensor, a monoclonal stable cell line was
784 generated by first transfecting wildtype RBL-2H3 cells using
785 the transfection protocol described below and then selecting
786 for expression positive cells with the mammalian culture
787 selection antibiotic G418 (Gibco, 10131035) at 0.5 mg/ml.
788 Following selection, fluorescence-activated cell sorting (FACS)
789 at the Yale Flow Cytometry Facility is used to isolate and
790 choose single cell clones with optimal fluorescence levels for
791 imaging.

792 **Cell culture.** RBL-2H3 cells were cultured in Minimum
793 Essential Medium (Gibco, 11095098) supplemented with 20%
794 fetal bovine serum (Millipore Sigma, F4135). Cell cultures are
795 allowed to grow between 1 to 4 days in either T25 (Corning,
796 430439) or T75 (Falcon, 353136) flasks with vented caps
797 maintained in a humidified 5% CO₂ incubator at 37 °C.
798 The maximum number of cell culture passages used in our
799 experiments was limited to 30.

800 **Transfection.** The Neon electroporation transfection system
801 (Invitrogen, MPK5000) with the 10 ml kit (Invitrogen,
802 MPK1025) is used for all experiments performed in this paper.

803 RBL-2H3 cells were disassociated from tissue culture flasks
804 using Trypsin-EDTA 0.25% (Gibco, 25200056), pelleted at
805 200g on a tabletop centrifuge and then resuspended in 2 mL
806 of MEM medium. Cell density of the resuspended cell solution
807 is determined with a hemacytometer (Marienfeld, 0640010).
808 Unless indicated otherwise, all samples were prepared by
809 transfecting 1.5 × 10⁶ cells with 1 μg of DNA plasmid
810 through electroporation with two 20 ms pulses at 1200 V.
811 Electroporated cells are then plated on 35 mm glass bottom
812 dishes (MatTek, P35G-1.5-20-C) and sensitized overnight
813 with 0.5 μg/ml of monoclonal anti-DNP IgE antibodies.
814

815 **Microscopy.** Before imaging, cells were washed three times
816 with pre-heated Tyrode's buffer [20 mM HEPES (pH = 7.4),
817 135 mM NaCl, 5.0 mM KCl, 1.8 mM CaCl₂, 1.0 mM MgCl₂,
818 5.6 mM glucose, 280–320 mOsm/kg H₂O] and transferred
819 to the on-stage incubator system (Live Cell Instrument)
820 maintained at 37 °C with humidity control. The cell sample
821 is allowed to equilibrate with the on stage incubator to
822 prevent thermal drift. Total internal reflection fluorescence
823 (TIRF) imaging is performed using a Nikon Eclipse Ti2
824 inverted microscope with three laser lines (488 nm, 561
825 nm, 643 nm). Laser power used varies with the type of
826 fluorescent probe in the sample. An motorized circular
827 TIRF illuminator (iLas 2 from Gataca Systems) is used
828 to ensure even evanescent wave generation. Images are
829 acquired with Nikon objectives (Apo TIRF 100x, N.A. 1.49
830 oil and 60x, N.A. 1.49 oil) and a back illuminated CMOS
831 Prime 95B camera (Teledyne Photometrics, 40fps @ 16 bit,
832 pixel size 11 μm by 11 μm). The microscope is controlled
833 by Metamorph software (MetaMorph Inc, Nashville). For
834 sequential TIRF and Differential interference contrast (DIC)
835 imaging, channel transition is modulated by the Multiple
836 Dimension Acquisition module in Metamorph and a Normaski
837 primary prism in the condenser. All imaging experiments
838 are performed at 37 °C, 5% CO₂ and appropriate humidity
839 levels maintained with an on-stage incubator system (Live
840 Cell Instrument, model CU-501 with 5 channels). Image
841 stacks are acquired at 0.5 to 4 second intervals with 50–150
842 ms exposure, depending on the conditions of the cell sample.

843 **Antigen stimulation.** A working solution of 200 ng/ml DNP-
844 BSA is prepared in Tyrode's buffer (recipe indicated above)
845 from a stock solution of 800 μg/ml DNP-BSA stored at -
846 20 °C. The working solution is preheated to 37 °C in a
847 polypropylene tube using a block heater for 10 minutes or
848 more. After the cell sample has equilibrated in the stage
849 incubator, 1 ml of the DNP-BSA working solution is added
850 to the MatTek dish containing 1 ml of buffer, creating a
851 final concentration of 100 ng/ml DNP-BSA. Traveling waves
852 of iRFP-P4M in stimulated RBL cells can be most readily
853 observed 30 to 120 minutes after DNP-BSA stimulation.

854 **Image analysis.** The acquired image stacks were in 16-bit
855 format, where each pixel maps to 0.18 μm or 0.11 μ in real
856 space when a 60x or 100x objectives are used respectively.
857 Image stacks were analyzed using a combination of built-
858 in and custom-written routines in Python (version 3.10.12,
859 Anaconda distribution), MATLAB (R2023b, MathWorks),
860 and Fiji (version 2.3.0/1.53t, ImageJ distribution).

861 **Data and code availability.** All original image analysis code
862 will be deposited in a GitHub repository and will be publicly
863 available.

available as of the date of publication. Data sets will be available upon reasonable request.

ACKNOWLEDGMENTS. We gratefully acknowledge Ding Xiong for initiating the PI(4)P project and the work done to discover PI(4)P oscillations. We thank Joe Howard, Mike Murrell, Ben Machta and members of the Wu lab for discussions and feedback. This work is supported by the Yale University Startup Fund (M.W.)

and the National Institute of General Medical Sciences of the National Institutes of Health under award number R01GM151344 (M.W.). The content is solely the responsibility of the authors and does not necessarily represent the official views of the National Institutes of Health. X.J.X. acknowledges support from the Yale Department of Physics and the Integrated Program in Physics, Engineering, and Biology (NSF 2012406).

1. GD Paolo, PD Camilli, Phosphoinositides in cell regulation and membrane dynamics. *Nature* **443**, 651–657 (2006).
2. T Balla, Phosphoinositides: Tiny Lipids With Giant Impact on Cell Regulation. *Physiol. Rev.* **93**, 1019–1137 (2013).
3. WD Heo, et al., PI(3,4,5)P3 and PI(4,5)P2 Lipids Target Proteins with Polybasic Clusters to the Plasma Membrane. *Science* **314**, 1458–1461 (2006).
4. MA Lemmon, Membrane recognition by phospholipid-binding domains. *Nat. Rev. Mol. Cell Biol.* **9**, 99–111 (2008).
5. EJ Dickson, B Hille, Understanding phosphoinositides: rare, dynamic, and essential membrane phospholipids. *The Biochem. journal* **476**, 1–23 (2019).
6. Y Posor, W Jang, V Hawcke, Phosphoinositides as membrane organizers. *Nat. Rev. Mol. Cell Biol.* **23**, 797–816 (2022).
7. T Sasaki, et al., Mammalian phosphoinositide kinases and phosphatases. *Prog. Lipid Res.* **48**, 307–343 (2009).
8. RL Doughman, AJ Firestone, RA Anderson, Phosphatidylinositol Phosphate Kinases Put PI4,5P2 in Its Place. *The J. Membr. Biol.* **194**, 77–89 (2003).
9. F Nakatsu, et al., PtdIns4P synthesis by PI4KIII α at the plasma membrane and its impact on plasma membrane identity. *J. Cell Biol.* **199**, 1003–1016 (2012).
10. GRV Hammond, et al., PI4P and PI(4,5)P₂ Are Essential But Independent Lipid Determinants of Membrane Identity. *Science* **337**, 727–730 (2012).
11. N Bojjireddy, et al., Pharmacological and Genetic Targeting of the PI4KA Enzyme Reveals Its Important Role in Maintaining Plasma Membrane Phosphatidylinositol 4-Phosphate and Phosphatidylinositol 4,5-Bisphosphate Levels. *J. Biol. Chem.* **289**, 6120–6132 (2014).
12. GR Hammond, MP Machner, T Balla, A novel probe for phosphatidylinositol 4-phosphate reveals multiple pools beyond the Golgi. *J. Cell Biol.* **205**, 113–126 (2014).
13. EJ Dickson, JB Jensen, B Hille, Golgi and plasma membrane pools of PI(4)P contribute to plasma membrane PI(4,5)P2 and maintenance of KCNQ2/3 ion channel current. *Proc. Natl. Acad. Sci. United States Am.* **111**, E2281–E2290 (2014).
14. J Myeong, et al., Phosphatidylinositol 4,5-bisphosphate is regenerated by speeding of the PI 4-kinase pathway during long PLC activation. *J. Gen. Physiol.* **152** (2020).
15. J Chung, et al., PI4P/phosphatidylserine countertransport at ORP5- and ORP8-mediated ER - Plasma membrane contacts. *Science* **349**, 428–432 (2015).
16. M Sohn, et al., PI(4,5)P2 controls plasma membrane PI4P and PS levels via ORP5/8 recruitment to ER-PM contact sites. *J. Cell Biol.* **217**, 1797–1813 (2018).
17. RC Wills, et al., A novel homeostatic mechanism tunes PI(4,5)P2-dependent signaling at the plasma membrane. *J. Cell Sci.* **136** (2023).
18. JA Brill, GR Hille, M Scharer-Schuksz, MT Fuller, A phospholipid kinase regulates actin organization and intercellular bridge formation during germline cytokinesis. *Development* **127**, 3855–3864 (2000).
19. AG Batrouni, N Bag, H Phan, BA Baird, JM Baskin, A palmitoylation code controls PI4KIII α complex formation and PI(4,5)P2 homeostasis at the plasma membrane. *J. Cell Sci.* **135** (2021).
20. J Tan, JA Brill, Cinderella story: PI4P goes from precursor to key signaling molecule. *Critical Rev. Biochem. Mol. Biol.* **49**, 33–58 (2014).
21. Mds Santos, RMZG Naal, B Baird, D Holowka, Inhibitors of PI(4,5)P2 Synthesis Reveal Dynamic Regulation of IgE Receptor Signaling by Phosphoinositides in RBL Mast Cells. *Mol. Pharmacol.* **83**, 793–804 (2013).
22. U Basu, SS Balakrishnan, V Janardan, P Raghu, A PI4KIII α protein complex is required for cell viability during Drosophila wing development. *Dev. Biol.* **462**, 208–222 (2020).
23. M Kučka, et al., Calcium-Prolactin Secretion Coupling in Rat Pituitary Lactotrophs Is Controlled by PI4-Kinase Alpha. *Front. Endocrinol.* **12**, 790441 (2021).
24. M Wu, X Wu, PD Camilli, Calcium oscillations-coupled conversion of actin travelling waves to standing oscillations. *Proc. Natl. Acad. Sci.* **110**, 1339–1344 (2013).
25. R Wollman, T Meyer, Coordinated oscillations in cortical actin and Ca²⁺ correlate with cycles of vesicle secretion. *Nat. cell biology* **14**, 1261–9 (2012).
26. D Xiong, et al., Frequency and amplitude control of cortical oscillations by phosphoinositide waves. *Nat. Chem. Biol.* **12**, 159–166 (2016).
27. RC Wills, BD Goulden, GRV Hammond, Genetically encoded lipid biosensors. *Mol. Biol. Cell* **29**, 1526–1532 (2018).
28. SD Hansen, AA Lee, BR Duewell, JT Groves, Membrane-mediated dimerization potentiates PIP5K lipid kinase activity. *eLife* **11** (2022).
29. BH Falkenburger, JB Jensen, B Hille, Kinetics of PIP2 metabolism and KCNQ2/3 channel regulation studied with a voltage-sensitive phosphatase in living cells. *J. Gen. Physiol.* **135**, 99–114 (2010).
30. Z Szentpeteri, P Várnai, T Balla, Acute manipulation of Golgi phosphoinositides to assess their importance in cellular trafficking and signaling. *Proc. Natl. Acad. Sci.* **107**, 8225–8230 (2010).
31. J Chung, F Nakatsu, JM Baskin, PD Camilli, Plasticity of PI4KIII α interactions at the plasma membrane. *EMBO reports* **16**, 312–320 (2015).
32. MR Hokin, LE Hokin, ENZYME SECRETION AND THE INCORPORATION OF P32 INTO PHOSPHOLIPIDES OF PANCREAS SLICES. *J. Biol. Chem.* **203**, 967–977 (1953).
33. RF Irvine, A short history of inositol lipids. *J. lipid research* **57**, 1987–1994 (2016).
34. R Rohatgi, et al., The interaction between N-WASP and the Arp2/3 complex links Cdc42-dependent signals to actin assembly. *Cell* **97**, 221–231 (1999).
35. R Rohatgi, Hy Ho, MW Kirschner, Mechanism of N-Wasp Activation by Cdc42 and Phosphatidylinositol 4,5-Bisphosphate. *The J. Cell Biol.* **150**, 1299–1310 (2000).
36. Y Yang, D Xiong, A Pipatsouk, OD Weiner, M Wu, Clathrin Assembly Defines the Onset and Geometry of Cortical Patterning. *Dev. Cell* **43**, 507–521.e4 (2017).
37. E Brombacher, et al., Rab1 guanine nucleotide exchange factor Sidm1 is a major phosphatidylinositol 4-phosphate-binding effector protein of Legionella pneumophila. *The J. biological chemistry* **284**, 4846–56 (2009).
38. GR Hammond, T Balla, Polyphosphoinositide binding domains: Key to inositol lipid biology. *Biochimica et Biophys. Acta (BBA) - Mol. Cell. Biol. Lipids* **1851**, 746–758 (2015).
39. O Ideval-Hagren, PD Camilli, Detection and manipulation of phosphoinositides. *Biochimica et Biophys. Acta (BBA) - Mol. Cell. Biol. Lipids* **1851**, 736–745 (2015).
40. GRV Hammond, MMC Ricci, CC Weckerly, RC Wills, An update on genetically encoded lipid biosensors. *Mol. Biol. Cell* **33**, 2015 (2022).
41. A Audhya, M Foti, SD Emr, Distinct roles for the yeast phosphatidylinositol 4-Kinases, Stt4p and Ptk1p, in secretion, cell growth, and organelle membrane dynamics. *Mol. Biol. Cell* **11**, 2673–2689 (2000).
42. A Audhya, SD Emr, Stt4 PI 4-Kinase Localizes to the Plasma Membrane and Functions in the Pkc1-Mediated MAP Kinase Cascade. *Dev. Cell* **2**, 593–605 (2002).
43. A Balla, G Tymetova, A Tsionenko, P Várnai, T Balla, A plasma membrane pool of phosphatidylinositol 4-phosphate is generated by phosphatidylinositol 4-kinase type-III alpha: Studies with the PH domains of the oxysterol binding protein and FAPP1. *Mol. Biol. Cell* **16**, 1282–1295 (2005).
44. A Balla, T Balla, Phosphatidylinositol 4-kinases: old enzymes with emerging functions. *Trends Cell Biol.* **16**, 351–361 (2006).
45. JA Lees, et al., Architecture of the human PI4KIII α lipid kinase complex. *Proc. Natl. Acad. Sci.* **114**, 13720–13725 (2017).
46. GL Dornan, et al., Probing the Architecture, Dynamics, and Inhibition of the PI4KIII α /TTC7/FAM126 Complex. *J. Mol. Biol.* **430**, 3129–3142 (2018).
47. R Rohatgi, et al., The interaction between N-WASP and the Arp2/3 complex links Cdc42-dependent signals to actin assembly. *Cell* **97**, 221–231 (1999).
48. XL Chua, et al., Competition and synergy of Arp2/3 and formins in nucleating actin waves. *Cell reports* **43**, 114423 (2024).
49. T Sakurai, et al., A conserved PI(4,5)P2-binding domain is critical for immune regulatory function of DOCK8. *Life Sci. Alliance* **4** (2021).
50. JL Johnson, JW Erickson, RA Cerione, C-terminal Di-arginine Motif of Cdc42 Protein Is Essential for Binding to Phosphatidylinositol 4,5-Bisphosphate-containing Membranes and Inducing Cellular Transformation. *J. Biol. Chem.* **287**, 5764–5774 (2012).
51. MC Armstrong, et al., The biochemical mechanism of Rho GTPase membrane binding, activation and retention in activity patterning. *The EMBO J.* pp. 1–38 (2025).
52. P Nalbant, L Hodgson, V Kravyn, A Touckhine, KM Hahn, Activation of endogenous Cdc42 visualized in living cells. *Science* **305**, 1615–1619 (2004).
53. SYS Fung, XJ Xú, M Wu, Nonlinear dynamics in phosphoinositide metabolism. *Curr. Opin. Cell Biol.* **88** (2024).
54. SD Hansen, et al., Stochastic geometry sensing and polarization in a lipid kinase-phosphatase competitive reaction. *Proc. Natl. Acad. Sci. United States Am.* **116**, 15013–15022 (2019).
55. F Brauns, E Frey, Self-organisation of protein patterns in *Active Matter and Non-Equilibrium Statistical Physics*, eds. J Tailleur, G Gompper, MC Marchetti, JM Yeomans, C Salomon. (Oxford University Press, Oxford, UK) Vol. 112, (2022).
56. SH Strogatz, *Nonlinear Dynamics and Chaos: With Applications to Physics, Biology, Chemistry, and Engineering.* (CRC Press, Boca Raton, FL), 3rd edition, 2nd Edition. (Springer New York, (2003).
58. M Ajiki, et al., ORP9-PH domain-based fluorescent reporters for visualizing phosphatidylinositol 4-phosphate dynamics in living cells. *RSC Chem. Biol.* **5**, 544–555 (2024).
59. Y Saheki, PD Camilli, Endoplasmic Reticulum—Plasma Membrane Contact Sites. *Annu. Rev. Biochem.* **86**, 1–26 (2017).
60. WA Prinz, A Toulmay, T Balla, The functional universe of membrane contact sites. *Nat. Rev. Mol. Cell Biol.* **21**, 7–24 (2020).
61. KM Reinisch, PD Camilli, TJ Melia, Lipid Dynamics at Membrane Contact Sites. *Annu. Rev. Biochem.* (2025).
62. D Xiong, C Tong, Y Yang, J Yong, M Wu, Constitutive, calcium-independent endoplasmic reticulum-plasma membrane contact site oscillations and its implications in store-operated calcium entry. *bioRxiv* p. 2022.03.30.486443 (2022).
63. D Xiong, C Tong, Y Yang, J Yong, M Wu, STIM1 and Endoplasmic Reticulum-Plasma Membrane Contact Sites Oscillate Independently of Calcium-Induced Calcium Release. *bioRxiv* p. 2025.03.16.643575 (2025).

993	64. WM Bement, AB Goryachev, AL Miller, Gv Dassow, Patterning of the cell cortex by Rho GTPases. <i>Nat. Rev. Mol. Cell Biol.</i> 25 , 290–308 (2024).	1055
994	65. O Ideval-Hagren, EJ Dickson, B Hille, DK Toomre, PD Camilli, Optogenetic control of phosphoinositide metabolism. <i>Proc. Natl. Acad. Sci. United States Am.</i> 109 (2012).	1056
995		1057
996		1058
997		1059
998		1060
999		1061
1000		1062
1001		1063
1002		1064
1003		1065
1004		1066
1005		1067
1006		1068
1007		1069
1008		1070
1009		1071
1010		1072
1011		1073
1012		1074
1013		1075
1014		1076
1015		1077
1016		1078
1017		1079
1018		1080
1019		1081
1020		1082
1021		1083
1022		1084
1023		1085
1024		1086
1025		1087
1026		1088
1027		1089
1028		1090
1029		1091
1030		1092
1031		1093
1032		1094
1033		1095
1034		1096
1035		1097
1036		1098
1037		1099
1038		1100
1039		1101
1040		1102
1041		1103
1042		1104
1043		1105
1044		1106
1045		1107
1046		1108
1047		1109
1048		1110
1049		1111
1050		1112
1051		1113
1052		1114
1053		1115
1054		1116



Supporting Information for

Distinct impact of PI(4)P flux in regulating PI(4,5)P₂ steady states and oscillations

X. J. Xu, C. S. Tong and M. Wu

This PDF file includes:

Supporting text
Figs. S1 to S3
Table S1
SI References

Supporting Information Text

1. Methods

A. Representative regions of interest (ROI). Unless otherwise indicated, ROI are by default chosen to be 20 by 20 pixels. We show further details on choosing representative regions in an image stack movie (Fig. S1). Within the middle of the adherent cell, away from the edge of the cell, the period map shows a region where the oscillation period is homogeneous. Thus the FFT dominant spectral peak of a times series is generally independent of the choice of ROI. For experiments in this paper, we perform spatial analysis for each cell to ensure that cell edge effects are not a confounding factor.

B. Fluorescence normalization. Fluorescence intensity plots are normalized by the whole cell fluorescence level. Time-lapse fluorescence movies are acquired as 16-bit grayscale TIFF stacks and processed with scikit-image (1) and Numpy (2) packages in Python. Fluorescence intensity time series u of a given region of interest (ROI) is normalized by

$$u' = \frac{u - u_0}{\bar{u} - u_0} \quad [B.1]$$

where u is the raster intensity value averaged over the ROI area; u_0 is the background fluorescence intensity from an equal size ROI adjacent to the cell of interest; \bar{u} is the mean value of u . This normalization method is intended to account for cell-to-cell variations in fluorescent sensor expression levels.

C. Kymograph generation. For the generation of displayed kymographs, custom Python code and Fiji software (3) were utilized. Through Fiji, the ‘reslice’ tool and ‘average projection filter’ were applied to generate the kymographs. To create each kymograph, 1-10 slices were used to generate the average projection. The Python code used to generate kymographs will be publicly available upon request.

D. Peak identification. For the determination of inter-peak intervals, individual peaks were identified based on secondary derivatives. The individual peaks were aligned at peak positions, and average curves were generated to obtain rise and drop phases.

E. Discrete Fourier transform. The fluorescence time series is given by an array $\{x_n\} = \{x_0, x_1, \dots, x_N\}$. The discrete Fast Fourier transform is

$$y_k = \sum_{n=0}^{N-1} e^{-2\pi i \frac{k}{N}} x_n \quad [E.1]$$

where the transformed array $\{y_k\} = \{y_0, y_1, \dots, y_N\}$ is in the frequency k space. The periods are given by the inverse frequency $T = 1/k$.

F. Cross-correlation analysis. Given two 1-dimensional sequences u and v , we computed their cross-correlation with the following function

$$c_k = \sum_n u_{n+k} \cdot \bar{v}_n \quad [F.1]$$

where k is the lag and \bar{v} denotes the complex conjugate. For auto-correlations, substitute \bar{v} for \bar{u} .

G. Wavelet transform. We performed a 1-D continuous wavelet transform on the oscillatory Rho signal $x(t)$

$$W(t, s) \equiv \int_{-\infty}^{\infty} \frac{1}{s} \psi^* \left(\frac{u-t}{s} \right) x(u) du \quad [G.1]$$

where $\psi(t)$ is the analyzing function - wavelet; s is the scale so $1/s$ effectively serve as the normalization factor in place of the typical $1/\sqrt{s}$ seen in Fourier transforms. The analytic Morse wavelet is utilized and is given by the following generalized form in frequency ω domain.

$$\Psi_{\beta, \gamma}(\omega) = U(\omega) a_{\beta, \gamma} \omega^\beta e^{-\omega^\gamma}$$

where U is the Heaviside step function; a is a normalization constant; while β and γ are the ‘decay’ and symmetry parameters respectively. The sampling frequency is set by the experimental image acquisition interval. The power spectrum of oscillation period is plotted alongside the same oscillation trace.

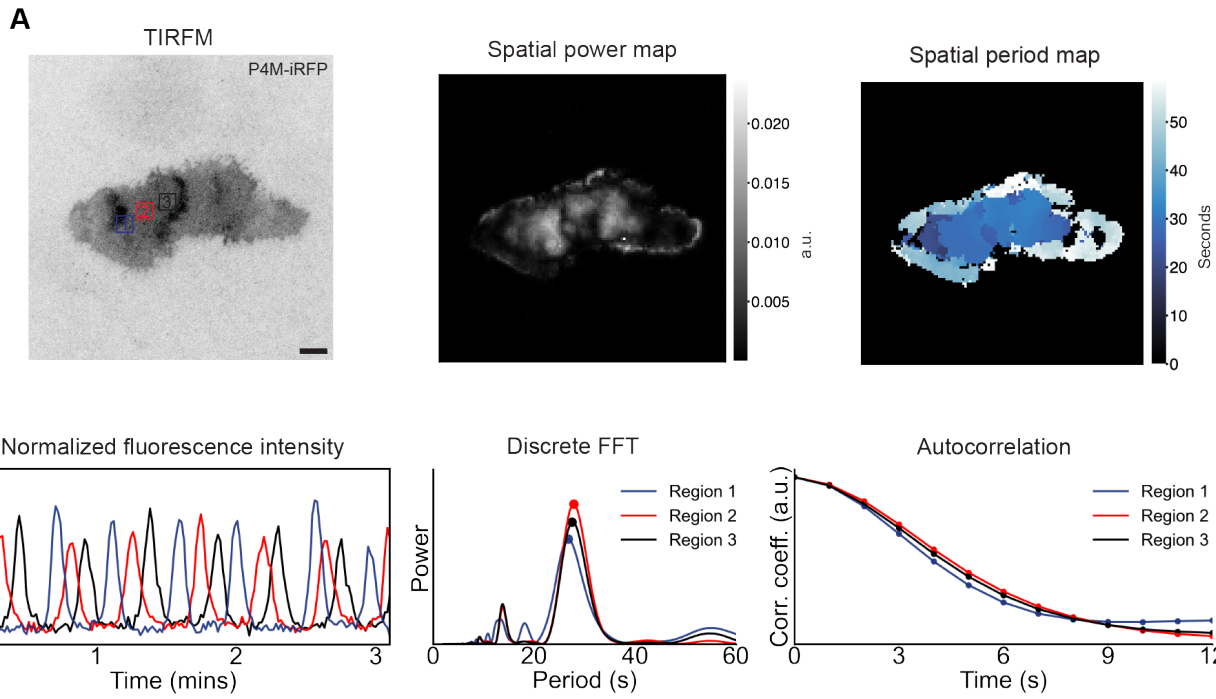


Fig. S1. Spatiotemporal analysis of PI(4)P traveling waves. (A) Left: TIRFM image showing P4M traveling waves on a mast cell expressing P4M-iRFP and labels indicate three regions of interest. Center and right: Spatial power and period maps show the spatial distribution of PI(4)P oscillations via fast Fourier transform of discretized bins of the image stacks. (B) Quantification of periodic traveling waves of the PI(4)P sensor made from P4M domain of SidM. Left: Fluorescence intensity plots of different regions on the plasma membrane display phase-shifted oscillations. Center: Power spectrum analysis based on fast Fourier transform shows that the three phase-shifted regions have the same peak periodicities 27.4 ± 0.5 seconds. Right: autocorrelation analysis verifies the existence of a periodic oscillation. Scale bars: 10 μm for micrographs.

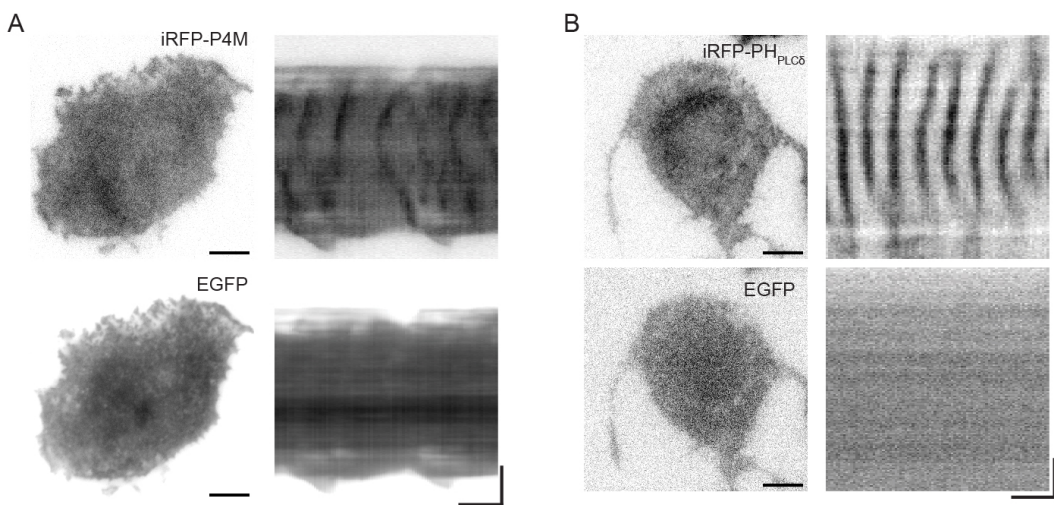


Fig. S2. PI(4)P and PI(4,5)P₂ sensor traveling waves with cytosolic control. (A) Micrographs and kymographs showing iRFP-P4M alongside cytosolic EGFP control. Scale bars: 10 μm for micrographs. (B) Micrographs and kymographs showing iRFP-PH_{PLC} δ alongside cytosolic EGFP control. For both sub-figures, the respective lipid sensor and EGFP plasmids are co-transfected into RBL cells and TIRF imaging is done 16-24 hours later. Scale bars: 10 μm for micrographs; 10 μm vertical and 1 minute horizontal for kymographs.

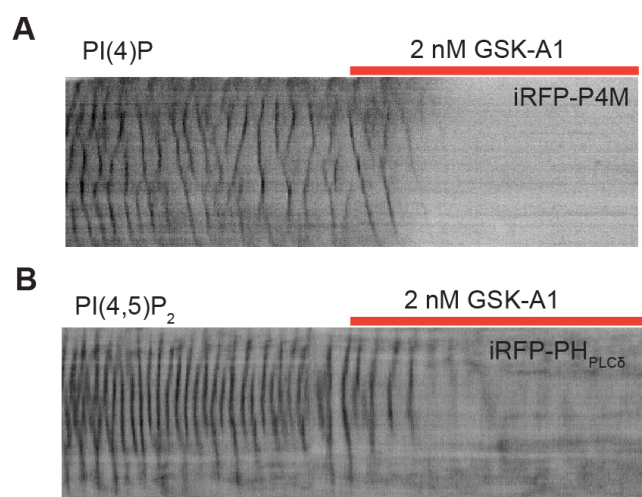


Fig. S3. Kymographs of PI(4)P and PI(4,5)P₂ sensor traveling waves under GSK-A1 inhibition. Kymographs of (A) iRFP-P4M and (B) iRFP-PH_{PLCδ} sensor traveling waves corresponding to Fig. 3B-C. Both kymographs are generated by vertical lines at the center of the cell. More details of kymograph generation are outlined in the Methods Section.

Table S1. Statistics for the experimental replicates used in figures and the corresponding experimental conditions.

Figure	Replicates		Condition
	Experiments	Cells	
1 & 2a & S1	5	20	30-120
3b & S2a	4	6	25-40
3c & S2b	4	5	14-48
4b	4	30	15-112
4c	4	9	15-60
5a & 4d	4	4	8-73
5b	3	5	15-41
5c	6	16	20-60

References

1. S Van der Walt, et al., scikit-image: image processing in Python. *PeerJ* **2**, e453 (2014).
2. CR Harris, et al., Array programming with NumPy. *Nature* **585**, 357–362 (2020).
3. J Schindelin, et al., Fiji: an open-source platform for biological-image analysis. *Nature Methods* **9**, 676–682 (2012).